Two-dimensional numerical modeling suggests preferred geometry of intersecting seismogenic faults

Abhijit Gangopadhyay and Pradeep Talwani

Department of Geological Sciences, University of South Carolina,

Columbia, South Carolina 29208, U.S.A.

ABSTRACT

A parametric study, using a two-dimensional Distinct Element Method, is carried out to investigate if there is a preferred geometry of intersecting faults that may favor the occurrence of intraplate earthquakes. Two and three vertical, intersecting faults within a block are subjected to a horizontal force across them, that represents the maximum horizontal compression (S_{Hmax}). The main fault is oriented at an angle α with respect to S_{Hmax} and β is the interior angle between the main fault and the intersecting fault. The third fault is oriented parallel to the main fault and is half its length. The distribution of shear stresses is examined along the faults for different values of α and β, and varying lengths of the main and intersecting faults. In all cases, maximum shear stresses are generated at the fault intersections. The modeling results reveal that the magnitude of the shear stresses depend on the values of α and β, with an optimum range for α, lying between 30° and 60°. In the case where the sign of the shear stress on the intersecting fault is opposite that on the main fault, the largest stresses at the fault intersections are obtained when β lies between 65° and 125°. When the stresses on these two faults are of the same sign, the largest stress values at the intersections are obtained when $145° \leq \beta \leq 170°$. The results of the modeling are consistent with the observed geometry of faults in the New Madrid and Middleton Place Summerville Seismic Zones.

INTRODUCTION

Intersecting faults have been postulated to play an important role in earthquake mechanics because they interact dynamically, and are sometimes responsible for controlling nucleation, dimension, propagation, and termination of earthquake ruptures (e.g. Sharp et al., 1982; Harris and Day, 1993; Rousseau and Rosakis, 2003; Spotila and Anderson, 2004). Hence, mechanics of intersecting faults and fault junctions have been extensively studied for decades (e.g. King and Nabelek, 1985; Pollard and Segall, 1987; McCaig, 1988; Andrews, 1989; Harris and Day, 1993; Andrews, 1994; Robinson and Benites, 1995; Maerten, 2000; Kato, 2001; Fitzenz and Miller, 2001; Crider and Peacock, 2004). However, most of these studies were directed towards understanding the role of intersecting faults in plate boundary earthquakes. A spatial association of intersecting faults with continental intraplate earthquakes was also observed (e.g. Talwani et al., 1979; Illies, 1982; King and Nabelek, 1985; King, 1986; Talwani, 1988) and, a causal association was proposed (Talwani, 1988; Talwani and Rajendran, 1991; Gangopadhyay and Talwani, 2003). Schematic and two-dimensional, linear-elastic and isotropic models to explain the cause of intraplate earthquakes in compressional stress regimes demonstrated that intersecting faults can act as stress concentrators and are spatially correlatable with the locations of observed intraplate seismicity (Talwani, 1988; Jing and Stephansson, 1990; Gangopadhyay et. al., 2004; Gangopadhyay and Talwani, 2005). However, geologic data show that intersecting faults are abundant in nature (McCaig, 1988), but only some of them are the locations of intraplate seismicity. This leads to the question whether there is a preferred geometry of intersecting faults that favors the occurrence of continental intraplate earthquakes. Earlier research involving field observations and analytical computations showed that there is a range of re-activation angles for pre-existing *Andersonian* thrust, normal, and strike-slip faults

using the commonly used Coulomb failure criteria and Byerlee-type values of static friction (Sibson, 1985; 1990; 1991). However, the effect of a compressional stress field on sets of two or more intersecting faults in intraplate regions has not been considered. Because intersecting faults are abundant, we address this question with a parametric study using 2-D numerical models. In this paper, our main effort is to investigate if there are configurations of faults which will optimally respond to plate tectonic stresses, concentrate stresses locally, and thus potentially play a role in the initiation of seismicity within plates. We are not attempting to explain the genesis of faulting over an earthquake cycle, or duplicating real situations. We do not address the effect of fluid pressures, and variations in frictional properties, parameters which can influence the likelihood of seismicity. This paper is mainly aimed at studying if there are preferred orientations of two or three intersecting faults with respect to S_{Hmax} and each other, that maximize local concentration of stresses, and if so, determining their optimal geometrical configurations. Our approach is described next.

NUMERICAL MODELING METHODOLOGY

Two-dimensional Distinct Element modeling is performed using a program called Universal Distinct Element Code (UDEC) written by Itasca Consulting Group, Inc., Minneapolis, MN (Version 3.1, 1999). This 2-D numerical program was first developed by Cundall (1971). The advantage of the Distinct Element Method over typical continuum based methods is its ability to change and update joint patterns continuously during the computation process (Jing and Hudson, 2002; Gangopadhyay et al., 2004). The program simulates the response of the discontinuous media to either static or dynamic loading. It models the rock mass as an assemblage of rigid or deformable discrete blocks and the faults as discontinuities. The

equations of motion for the blocks are solved by a central difference scheme and mutual interactions between blocks are included. It uses calculations in the Lagrangian scheme to model large movements and deformations of a system. Several built-in material behavior models, for both the intact blocks and the faults, permit the simulation of real geologic situations. Displacements are allowed along the faults, which are treated as boundaries between blocks, allowing the blocks to move with respect to each other. The individual blocks can be made either rigid or deformable. The deformable blocks are divided into a mesh of triangular constant-strain finite difference zones and each zone behaves according to a prescribed stress-strain law. In the case of elastic analysis the formulation of these zones is identical to that of constant-strain finite elements. The relative motions along the discontinuities are constrained by force-displacement relations for movement in both the normal and shear directions. The suitability, efficiency, and adaptability of UDEC in solving two-dimensional, simplified geological problems involving faulted and fractured rocks has been adequately demonstrated and established (see e.g. Gangopadhyay et al., 2004 and references therein). For example, it was used to model tectonic and geologic frameworks of active intraplate regions in New Madrid (Gangopadhyay et al., 2004) and Charleston (Gangopadhyay and Talwani, 2005).

DEVELOPMENT OF THE 2-D MODEL

Model Geometry

Examination of 20 case histories of intraplate regions globally that have been host to 39 earthquakes of M 5.0 or greater, revealed that 65% of them comprised of two or three intersecting faults, which acted as stress concentrators and location of intraplate earthquakes (Gangopadhyay and Talwani, 2003). Thus, in this parametric study we model tectonic

4

frameworks consisting of two and three intersecting faults. Figure 1 shows the block geometries for these two frameworks. They are strictly two-dimensional. The maximum horizontal compressive stress, S_{Hmax} is oriented E - W in all cases. The block is compressed by a force applied along the x-axis. This force is along the inferred direction of plate motion and its magnitude is proportional to the plate velocity discussed in detail in the next section. In this case, the main fault, AB, subtends an angle α with the direction of S_{Hmax} and an interior angle β with the intersecting fault, BC (Figure 1). The blocks and faults have been made linear-elastic and associated with elastic properties that are detailed in a later section. In the first set of simulations with two intersecting faults, the length of the main fault (AB) is taken as 10 units and that of the intersecting fault (BC) is chosen to be 1, 3, and 5 units (Figure 1a). A similar set of simulations with two intersecting faults is carried out with length of AB = 10 units and oriented at an angle $(180° - \alpha)$ and length of BC = 3 units (Figure 1b). A third set of simulations are performed varying the length of AB (1, 3, and 5 units) and keeping BC fixed (10 units) (Figure 1c). In the case of three intersecting faults (Figure 1d), the length of the main fault is 10 units, a shorter fault CD is introduced with a length of 5 units and oriented parallel to the main fault. The lengths of faults AB and CD and the orientation of CD are kept fixed. The intersecting fault (BC) connects the two faults AB and CD (Figure 1d). Simulations of this model are performed with varying lengths of BC (1, 3, and 5 units). In all cases, the block corners are rounded with a circle that is tangential to the two corresponding edges at a specified rounding distance from the corner. In practice, the rounding distance is about 1% of the typical block edge length (UDEC Command Reference Manual, 1999) and the same is utilized in our model simulations. Since our model is two-dimensional the commonly used plane stress condition is imposed, wherein none of the

blocks experience stresses in the vertical direction although they can exhibit strain in that direction.

The computer code divides the deformable blocks into triangular finite difference zones using a built-in automatic mesh generator that decides the size of the zones based on the block lengths, specified rounding length, and the memory availability to perform the computations. All the blocks in our model are deformable and movable with respect to each other. UDEC calculates the amplitude and sign of the shear stress (τ_{xy}) at each node. Shear stress (τ_{xy}) is positive when it tends to rotate the block in a counter-clockwise manner, i.e. by left-lateral strike-slip, and negative when the block rotation is clockwise. The sign of the shear stress can be used to infer how the block will rotate and contours to show its spatial variation.

Model Parameters

UDEC has seven built-in constitutive models for the blocks and four for the joints that can represent various geologic situations. The simplest constitutive models are utilized for this parametric study. In our model the blocks conform to the Linearly Elastic Isotropic Model and the faults follow the Joint Area Contact Elastic/Plastic Coulomb Slip Failure Model. The Linearly Elastic Isotropic Model for the blocks describes the simplest form of material behavior assuming homogenous and isotropic materials that exhibit linear stress-strain behavior with reversible deformation upon unloading (UDEC Command Reference Manual, 1999). The Joint Area Contact Elastic/Plastic Coulomb Slip Failure Model for the joints is the most commonly used Coulomb slip model that predicts failure or initiation of slip on a fault based on the accumulated shear stress (UDEC Command Reference Manual, 1999). It is represented by the following equations:

$$\Delta\sigma_n = - k_n\Delta u_n$$

$$\Delta\tau_S = - k_S\Delta u_S$$

where, $\Delta\sigma_n$, Δu_n, $\Delta\tau_S$, and Δu_S are the effective normal stress, normal displacement, shear stress, and shear displacement increments respectively.

The failure criterion for the joints is given by,

$$|\tau_S| \geq C + \sigma_n\tan\phi$$

where τ_S = shear stress, C = cohesive strength of the joint, σ_n = normal stress, and ϕ = friction angle for the joint.

The block assembly is subjected to a horizontal compressive force along the x-axis. This is achieved by subjecting the right block boundary to a prescribed displacement resulting from a plate velocity of 5 mm/year. The left boundary is kept fixed. The plate velocity is determined from geodetic observations in two major active intraplate regions of eastern U.S. (see Gangopadhyay et al., 2004 for details). The calculated stresses scale linearly with velocity. The applied velocity gradient in our model is larger than those obtained from GPS measured velocities and was chosen in order to obtain a measurable response with a shorter loading time used in the computer model. The velocity gradient is also assumed to not be a function of depth and hence the whole block is subjected to the same horizontal stress.

Model Properties

Input modeling parameters are based on an earlier study involving the New Madrid Seismic Zone (NMSZ) (Gangopadhyay et al., 2004). Those values are considered to be representative of active intraplate regions. These properties and their derivations have been described in detail in that study. In our computations, we assume a value of 1.73, 5.63 km/s, and 2690 kg/m^3 for the V_P/V_S ratio, P-wave velocity, and density respectively for all the blocks in the

model. Utilizing these values we compute the bulk and shear moduli to be 47.28 GPa and 28.48 GPa respectively for the various blocks.

Other input parameters required for modeling the deformation include friction angle, normal and shear stiffnesses, and cohesion of the faults (treated as joints). The chosen values of these parameters are also from the NMSZ study (Gangopadhyay et al., 2004), viz., friction angles of 27°, and joint normal and shear stiffnesses of 101 GPa/m and 76 GPa/m respectively for all faults. The faults are considered to be cohesionless.

Limitations of the model

A notable limitation of this model is the fact that it is two-dimensional. Because it is a two-dimensional code, all faults are considered to be vertical and the effects in the third dimension can not be observed. The code does not allow us to study isolated faults within a block but require that faults be extended to block boundaries. However, the computational scheme in UDEC is such that when using a linear, elastic, and isotropic constitutive model, the effect of stress concentration at the boundaries have minimal effects at the fault intersections within the block. In spite of these limitations, by keeping the fault intersections away from the block boundaries it is possible to study the effects of their geometrical configurations on stress concentration and its possible influence on earthquake generation. Due to memory limitations in our version of UDEC program, it is not possible to run the model for a geologically realistic loading time. However, the model has been run for different loading times and the calculated stress was found to be linear with loading time, and thus running the model for shorter times provides relative stress distributions – the objective of this study. In this study, the model simulations are performed for 100,000 cycles (tectonic loading of 1 day). The results of our model simulations are described in the next section.

MODEL SIMULATION RESULTS

Outputs from the model simulations include normal and shear stresses developed in the blocks and along the faults. The shear stresses in response to the applied tectonic loading along the individual fault planes are analyzed. The absolute values of the shear stresses depend on the model parameters and tectonic loading time, and those obtained in this study are representative, however their relative values are more instructive. It is observed from the results of the different simulations that the shear stresses in plan view (Figure 2) are largest at the intersections of the faults (i.e. at B for faults AB and BC) (Figure 2a) and near C for fault CD (Figure 2b). Shear stresses are positive (Figure 2) when they tend to rotate the block in a counter-clockwise manner, i.e. by left-lateral strike-slip, and negative when the block rotation is clockwise. Shear stresses are also obtained along the faults and the model simulation results discussed below show the variation of shear stresses at B along AB and BC, and at C along CD for a range of values of α, β, and the length of BC. The results are presented in two sections, first, the case of two intersecting faults and second, the case of three intersecting faults. For purposes of clarity, the variation of the magnitude of shear stresses for different values of α for each set of simulations is shown in two diagrams.

Case I – Two intersecting faults

The simulations with two intersecting faults are performed using three different block geometries shown in Figures 1a – 1c. The main results of all the simulations are presented in Table 1. The first block geometry comprise of a main fault AB of length 10 units and an intersecting fault BC (Figure 1a). The model is run with α ranging between 20° to 80° and β ranging between 20° to 160° in increments of 20° for each value of α, with an additional value at β = 175°. Three sets of simulations are carried out, varying the length of BC (1, 3, and 5 units).

The shear stresses at the intersection B along the fault planes AB and BC are observed for each set and tabulated (Table 1). They are negative when the motion along the fault is right-lateral (α and γ are acute angles with respect to S_{Hmax}) and positive when the motion along the fault is left-lateral (α and γ are obtuse angles with respect to S_{Hmax}) (Table 1, Figures 1a and 1b). The data presented in the table are illustrated using one example, with AB as 10 units, and BC, 3 units long. Shear stresses are calculated at B along AB (Figures 3 a, b) and at B along BC (Figures 3 c, d) for various values of α (different color curves) as a function of β. For clarity the results are presented separately for $\alpha < 45°$ (Figures 3a and 3c) and $\alpha \geq 45°$ (Figures 3b and 3d). In all cases, along AB, the calculated stresses are negative, implying right-lateral shear. For the first case, the maximum value of shear stress (-1.25 N/m^2) is obtained for $\alpha = 50°$ and $\beta = 80°$ (Figure 3b). We arbitrarily choose a "Favorable Range", where the stresses are $\geq 90\%$ of this maximum value. For the above-mentioned case (assuming linear variation between plotted angles), the favorable ranges are estimated from the curves for both α and β, and are found to be 46° to 53°, and 76° to 91° respectively. These are shown in Table 1. The shear stress at B along BC is found to be both positive and negative, depending on the orientation of BC with respect to S_{Hmax} (the angle γ, Figure 1a). A negative value (indicating right-lateral strike-slip along BC) occurs when $\gamma < 90°$, when $\beta >> 90°$ and BC essentially trends in the same direction as AB (Figure 1a). When $\gamma > 90°$, the shear stress on BC is positive indicating left-lateral shear. Correspondingly, two peaks in shear stress values, one positive and the other negative, are obtained for various combinations of α and β (Figures 3c and d). These two peaks yield maximum shear stress values and favorable ranges of α and β for left-lateral (positive shear stress) and right-lateral (negative shear stress) movement. These are listed in Table 1. The maximum shear stress at B along BC associated with the right-lateral motion is found to be -1.72 N/m^2 and it occurs at $\alpha = 40°$ and $\beta = 160°$ (Figure

10

3c). The peak shear stress at B along BC (in the left-lateral region, positive shear stress values) is 1.25 N/m^2 and occurs at $\alpha = 45°$ and $\beta = 100°$ (Table 1, Figure 3d). The favorable range is found to be 30° to 45° for α and 75° to 105° for β, whereas the favorable ranges for right-lateral motion are 37° to 41° and 153° to 170° for α and β respectively (Table 1). The results for the same geometry (Figure 1a) but for different lengths of BC (1 and 5 units) are presented in Table 1.

In simulations described above, the main fault AB is at an acute angle with S_{Hmax} (α ranged from 20° - 80°). The next simulation is performed for $\alpha > 90°$ (Figure 1b), with AB 10 units and BC 3 units long. The model is run with α ranging between 100° to 160° (or (180° - α) from 80° to 20°) and β ranging between 20° to 175° for each value of α. The shear stresses at the intersection B along the fault planes AB and BC are observed for each set, and the results are presented in Table 1. We note that the shear stresses at B along AB are positive for this geometry, indicating left-lateral motion along fault AB (Table 1). The largest shear stress at B along AB (1.32 N/m^2) occur for $\alpha = 130°$ (supplementary to 50°) at $\beta = 80°$ (Table 1). The estimated favorable ranges for α and β are 127° - 134° and 75° - 90° respectively. Along BC the shear stresses at B are both positive and negative (according as γ was $\geq 90°$ or $< 90°$) similar to the geometry in Figure 1a. As before, the positive values (corresponding to left-lateral shear) occur when $\beta \gg 90°$ and negative values for $\gamma < 90°$ (Table 1). Along BC in the right-lateral range, the largest shear stress (-1.18 N/m^2) occur for $\alpha = 145°$ (supplementary to 35°) at $\beta = 80°$, and the corresponding favorable ranges are 140° to 150° for α and 70° to 85° for β (Table 1). When the motion along BC is left-lateral, the maximum positive shear stress (1.64 N/m^2) occurs for $\alpha = 140°$ at $\beta = 160°$ and the corresponding favorable ranges for α and β are 137° - 143° and 152° - 170° respectively (Table 1). Note that in this simulation for comparison with the geometry

in Figure 1a, we measure the angle α with respect to S_{Hmax} oriented in the negative x-direction. The optimum value of α is found to lie between 127° and 134°. When comparing with other models (Figures 1a, c, and d) we compare the supplementary angle, i.e., the acute angle 53° to 46° between the fault and the S_{Hmax} oriented in the positive x-direction.

The block geometry shown in Figure 1c is used in the third model run with two intersecting faults. In these runs the length of fault AB is varied (1, 3, and 5 units) whereas the length of fault BC (10 units) is kept unchanged. The results of all the runs are summarized in Table 1. The maximum value of shear stress at B along AB (-1.32 N/m^2) is obtained for $\alpha = 45°$ and $\beta = 80°$ (Table 1). The favorable ranges are found to be 45° to 50°, and 70° to 84° for α and β, respectively (Table 1). Similarly, two peaks are found for the shear stresses at B along BC. In the left-lateral range, it is found to be 1.24 N/m^2 and it occurs at $\alpha = 30°$ and $\beta = 80°$ (Table 1) and the corresponding favorable range is found to be 30° to 35° for α and 72° to 84° for β (Table 1). In the right-lateral range, the maximum shear stress value is -1.8 N/m^2 which occurs for $\alpha = 40°$ and $\beta = 160°$ and the corresponding favorable ranges are 33° to 42° and 151° to 162° for α and β respectively (Table 1).

Case II – Three intersecting faults

For the case of three intersecting faults (Figure 1d), CD (5 units long) is oriented parallel to fault AB. In three model runs, the lengths of AB (10 units), and CD (5 units) are kept fixed, while that of BC is varied (1, 3, and 5 units). The angles α and β are varied in the same way as for the case with two intersecting faults and the shear stresses at the intersections B and C along fault planes AB, BC, and CD are observed. The results of the simulations are presented in Table 2 and those for the case where AB, BC, and CD are 10, 3, and 5 units long respectively are shown in Figure 4a – 4f, and are discussed below. The shear stresses are negative when the

12

motion along the fault is right-lateral (α and γ are acute angles) and positive when the motion along the fault is left-lateral (α and γ are obtuse angles) (Table 2). The largest shear stress at B along AB (-1.42 N/m^2) occur for $\alpha = 50°$ at $\beta = 80°$ (Figure 4b). As in the case of two intersecting faults, two peaks of shear stresses are observed at B along BC, one when $\gamma < 90°$ (right-lateral motion along BC) and the other when $\gamma \geq 90°$ (left-lateral motion along BC). Along BC in the left-lateral range, the maximum shear stress (1.32 N/m^2) occur for $\alpha = 35°$ at $\beta = 80°$ (Figure 4c), whereas in the right-lateral range, it is -1.8 N/m^2 for $\alpha = 40°$ at $\beta = 160°$ (Table 2). At C along CD, the largest shear stress (-1.39 N/m^2) occur for $\alpha = 50°$ at $\beta = 80°$ (Figure 4f) (Table 2). The estimated favorable ranges for α and β are 48° - 53° and 69° - 89° when observed along fault AB, 30° - 38° and 68° - 85° when observed along fault BC in the left-lateral range, 34° - 42° and 150° - 163° when observed along fault BC in the right-lateral range, and 48° - 56° and 76° - 103° when observed along fault CD respectively (Table 2).

Summarizing, all 12 favorable ranges of shear stresses (at B along AB and BC, and at C along CD) occur only when α lies between 30° and 60° (Table 2). Along AB and CD the favorable ranges of shear stresses are observed when α lies between 45° - 60°, whereas along BC the corresponding range for α is 30° - 45°. The favorable ranges of shear stresses along AB, BC (for left lateral movement) and CD are observed when β lies between 65° and 105° and for right-lateral movement along BC, when β lies between 145° - 166°.

In summary, from the results of model calculations for two and three intersecting faults (Tables 1 and 2) we note the following:

(a) The maximum shear stresses are generated at the fault intersections, B and C along the faults.

(b) Increasing the length of BC (keeping length of AB fixed) or increasing the length of AB (keeping length of BC fixed) results in an increase in the maximum shear stress at B.

(c) The larger shear stress at B is found to be along the shorter of the two intersecting faults AB and BC.

(d) Two peaks, one positive and one negative are obtained for the shear stress along BC at B. The sign of the shear stress is the same as that at B along AB for large values of β (γ << 90°), i.e., when BC is oriented essentially in the same direction as AB. When γ is > 90° the sign of shear stress at B along BC is opposite that at B along AB.

(e) In all cases, the favorable range for orientation of fault AB with respect to S_{Hmax} (α) is found to be ~30° - 60°. The largest shear stresses at B along AB are observed when 45° $\leq$ $\alpha \leq$ 60° and along BC when 30° $\leq \alpha \leq$ 45°.

(f) Along AB, CD, and BC (when the sign of the shear stress is opposite that along AB), the favorable range of shear stresses are obtained for β = 65° - 125°. In the case where the shear stresses along BC and AB are of the same sign, i.e., AB and BC are essentially along the same direction, the favorable range of shear stresses are obtained for β = 145° - 170°.

(g) The large favorable range of β (65° - 125°) for the case AB = 10 and BC = 1 units long is probably an artifact of the modeling, as B is close to the horizontal block boundary.

We test these results of simple 2-D models with observations from two active intraplate locations in eastern U.S.

DISCUSSION

The results of two-dimensional modeling presented above indicate that the magnitude of stress accumulation at fault intersections, subjected to plate tectonic forces, depends on their orientation with respect to S_{Hmax} and each other. They also suggest that there is an optimal fault geometry for their reactivation. The areal distribution of stress is instructive and can be compared with observed locations of seismicity associated with intersecting faults. However, the comparison is only limited to stress concentration in two-dimensions which may enhance the seismic potential of a region.

We compare our modeling results with observations from New Madrid Seismic Zone (NMSZ) and Middleton Place Summerville Seismic Zone (MPSSZ) near Charleston, South Carolina. Both these regions have been extensively studied and reliable information about their fault geometry is available.

Figure 5a shows the structural framework of NMSZ as outlined by Hildenbrand et al. (2001) and the instrumentally located earthquakes with M 3.0 or greater adapted from 1974 – 2002 CERI, Memphis catalog. In NMSZ, within the NE – SW trending, nearly 400 km long and 100 km wide Reelfoot rift, there are two intersecting fault zones, the ~65 km long Blytheville Fault Zone (BFZ) oriented ~NE – SW and the ~60 km long Reelfoot fault zone (RF) oriented NW - SE (Van Arsdale et al., 1995; Johnston and Schweig, 1996). A third fault, the New Madrid North fault (NMNF) lies outside the edge of floor of the Reelfoot rift but within its edge (Rhea and Wheeler, 1995). This ~30 km long NNE trending fault is considered to be the extension of the aseismic Bootheel lineament (BL) (Johnston and Schweig, 1996). The observed seismicity inside the Reelfoot rift is located along the Blytheville Fault Zone, Reelfoot, and the New Madrid North faults (Figure 5a) with a clustering of seismicity at and/or near the fault

intersections (Figure 5a). The direction of maximum horizontal stress, S_{Hmax} in the region is oriented N80°E (Figure 5; Zoback, 1992). The seismically active Blytheville Fault Zone (BFZ), and New Madrid North fault (NMNF) are oriented at 39° and 53° (α) with respect to S_{Hmax} respectively (Figure 5b). Pujol et al. (1997) and Mueller and Pujol (2001) have reanalyzed the seismicity associated with the Reelfoot fault. Based on their analyses, the Reelfoot fault (RF) has been divided into three segments that are oriented (from south to north) ~N28°W, ~N-S, and ~N36°W respectively (Figure 5b). The orientations (internal angles) of the southern segment with respect to the BFZ and of the NMNF with the northern segment of RF are found to be 111° and 117° (β) respectively (Figure 5b). If we treat the three segments as one Reelfoot fault, the angle between the Blytheville Fault Zone and Reelfoot fault range between ~110° - 120°. These angles (α and β) are within the preferred range obtained from this parametric study (i.e., $30° \leq \alpha \leq 60°$, $65° \leq \beta \leq 125°$). The BFZ and NMNF exhibit right-lateral motion whereas RF (oriented at an obtuse angle with S_{Hmax}) shows some left-lateral motion (Hermann and Ammon, 1997) consistent with the model results. Due to its two-dimensional nature, this model is incapable of replicating the predominantly reverse movement on RF.

The structural framework of MPSSZ is shown in Figure 6. The ~12 km long, ~NW – SE Sawmill Branch Fault (SBF) - Ashley River fault (ARF) system intersects the ~NNE trending Woodstock fault (WF) which is about 200 km long, dividing it into northern (WF(N)) and southern (WF(S)) legs (Figure 6; Dura-Gomez, 2004). The WF(N) trends ~N15°E – N28°E whereas the WF(S) which meets at the intersection of SBF – ARF system trends ~N30°E (Marple and Talwani, 2000; Dura-Gomez, 2004). The ~6 km long SBF is oriented N30°W whereas the ~6 km long ARF trends N60°W (Figure 6; Dura-Gomez, 2004). Only about a 30 km segment of the WF(N) near the intersection is active seismically (dashed circle in Figure 6). The

instrumentally located seismicity (1974 – 2004) in this region lies mostly along the SBF and is concentrated near its intersection with WF(N) and WF(S) (Figure 6). S_{Hmax} in the region is oriented N60°E (Figure 6; Talwani, 1982; Zoback, 1992). The orientations of the Woodstock fault (North) and (South) with respect to S_{Hmax} (α_1 and α_2) in MPSSZ are found to be 30° - 38° and 30° respectively (Figure 6). SBF subtends an internal angle of 120° (β) with both the WF(N) and WF(S) (Figure 6). Thus the range of angles between the seismogenic faults and S_{Hmax}, α, in MPSSZ is 30° - 38°, and the interior angle between the intersecting faults, β, is ~120°. These values are consistent with the results of the 2-D modeling (α between 30° - 60°, and β between 65° - 125°). Similar to NMSZ and matching our model results, in MPSSZ, WF(N) and WF(S) exhibit right-lateral motion whereas SBF (oriented at an obtuse angle with S_{Hmax}) exhibits some left-lateral motion, although the predominant movement on it is reverse. Due to its two-dimensional nature, this model is incapable of replicating any uplift motion.

CONCLUSIONS

In summary, the results of this parametric study suggest that when subjected to plate tectonic forces, only optimally oriented intersecting faults are reactivated due to a larger shear stress build-up, and thus may cause intraplate seismicity. The maximum shear stresses are generated at the fault intersection and increasing the length of the intersecting faults resulted in an increase in the maximum shear stress. The largest shear stress at an intersection is found to be along the shorter of the two intersecting faults. The favorable range for orientation of the main fault with respect to S_{Hmax} (α) is found to be ~30° - 60° (Figure 7). The largest shear stresses at the intersection along the main fault are observed when $30° \leq \alpha \leq 45°$ and along the intersecting

17

fault when $45° \leq \alpha \leq 60°$. The range of β that yields maximum shear stresses at the intersection is ~65° - 125° (Figure 7) when the motion along the intersecting fault is opposite that along the main fault. When the two faults have the same sense of motion, β is found to lie between 145° and 170° for favorable range of shear stresses. For the case of three intersecting faults, the optimum orientation of CD is the same as that for AB (Figure 7b).

In spite of the limitations and the two-dimensional nature of the models, by studying the fault geometries of intersecting faults and their orientation with respect to S_{Hmax} and each other it is possible to identify more likely seismogenic faults in the presence of the ambient stress field. Future studies will include a comparison of model results with orientations of seismogenic faults in other intraplate regions.

ACKNOWLEDGEMENTS

REFERENCES

Andrews, D. J., 1989, Mechanics of fault junctions: Journal of Geophysical Research, v. 94, p. 9,389 – 9,397.

Andrews, D. J., 1994, Fault geometry and earthquake mechanics: Annali Di Geofisica, v. 37, p. 1,341 – 1,348.

Crider, J. G., and Peacock, D. C. P., 2004, Initiation of brittle faults in the upper crust: a review of field observations: Journal of Structural Geology, v. 26, p. 691 – 707.

Cundall, P. A., 1971, A computer model for simulating progressive, large scale movement in blocky rock systems, *in* Proceedings, Symposium on Rock Fracture, I, Nancy: International Society of Rock Mechanics, p. II-8.

Dura-Gomez, I., 2004, Seismotectonic Framework of Middleton Place Summerville Seismic Zone, Charleston, South Carolina: M.S. Thesis, University of South Carolina, 180 p.

Fitzenz, D. D., and Miller, S. A., 2001, A forward model for earthquake generation on interacting faults including tectonics, fluids, and stress transfer: Journal of Geophysical Research, v. 106, p. 26,689 – 26,706.

Gangopadhyay, A., and Talwani, P., 2003, Symptomatic Features of Intraplate Earthquakes: Seismological Research Letters, v. 74, p. 863 – 883.

Gangopadhyay, A., Dickerson, J., and Talwani, P., 2004, A two-dimensional numerical model for the current seismicity in New Madrid Seismic Zone: Seismological Research Letters, v. 75, p. 406 – 418.

Gangopadhyay, A., and Talwani, P., 2005, Fault intersections and intraplate seismicity in Charleston, South Carolina: Insights from a 2-D numerical model: Current Science, v. 88, p. 1,609 – 1,616.

Harris, R. A., and Day, S. M., 1993, Dynamics of fault interaction: parallel strike-slip faults: Journal of Geophysical Research, v. 98, p. 4,461 – 4,472.

Herrmann, R. B., and Ammon, C. J., 1997, Faulting parameters of earthquakes in the New Madrid, Missouri, region: Engineering Geology, v. 46, p. 299 – 311.

Hildenbrand, T. G., Stuart, W. D., and Talwani, P., 2001, Geologic structures related to New Madrid earthquakes near Memphis, Tennessee, based on gravity and magnetic interpretations: Engineering Geology, v. 62, p. 105 – 121.

Illies, J. H., 1982, Der Hohenzollern Graben und Intraplatten-Seismizitat infolge Vergitterung lamellarer Scherung mit einer Riftstruktur. Oberrhein. Geol. Abh., v. 31, p. 47 – 78.

Jing, L., and Stephansson, O., 1990, Numerical modeling of intraplate earthquake source by 2-dimensional distinct element method: Gerlands Beitr. Geophysics, v. 99, p. 463 – 472.

Jing, L., and Hudson, J. A., 2002, Numerical methods in rock mechanics: International Journal of Rock Mechanics & Mining Sciences, v. 39, p. 409 – 427.

Johnston, A. C., and Schweig, E. S., 1996, The Enigma of the New Madrid Earthquakes of 1811 – 1812: Annual Reviews of Earth and Planetary Sciences, v. 24, p. 339 – 384.

Kato, N., 2001, Simulation of seismic cycles of buried intersecting reverse faults: Journal of Geophysical Research, v. 106, p. 4,221 – 4,232.

King, G., and Nabelek, J., 1985, Role of fault Bends in the Initiation and Termination of Earthquake Rupture: Science, v. 228, p. 984 – 987.

King, G. C. P., 1986, Speculations on the geometry of the initiation and termination processes of earthquake rupture and its relation to morphological and geological structure: Pure and Applied Geophysics, v. 124, p. 567 – 585.

Maerten, L., 2000, Variation in slip on intersecting normal faults: Implications for paleostress inversion: Journal of Geophysical Research, v. 105, p. 25,553 – 25,565.

Marple, R. T., and Talwani, P., 2000, Evidence for a buried fault system in the coastal plain of the Carolinas and Virginia – Implications for neotectonics in the southeastern United States. Geological Society of America Bulletin, v. 112, p. 200 – 220.

McCaig, A., 1988, Vector analysis of fault bends and intersecting faults: Journal of Structural Geology, v. 10, p. 121 – 124.

Mueller, K., and Pujol, J., 2001, Three-dimensional geometry of the Reelfoot Blind Thrust: Implications for moment release and earthquake magnitude in the New Madrid Seismic Zone: Bulletin of the Seismological Society of America, v. 91, p. 1,563 – 1,573.

Pollard, D. D., and Segall, P., 1987, Theoretical displacements and stresses near fractures in rock: with applications to faults, joints, veins, dikes, and solution surfaces, *in* Atkinson, B. K., ed., Fracture Mechanics of Rock: London, Academic Press, p. 277 – 349.

Pujol, J., Johnston, A., Chiu, J. M., Yang, Y. T., 1997, Refinement of thrust faulting models for the Central New Madrid seismic zone: Engineering Geology, v. 46, p. 281 – 298.

Rhea, S., and Wheeler, R. L., 1995, Map showing synopsis of seismotectonic features in the vicinity of New Madrid, Missouri: U.S. Geological Survey Miscellaneous Investigations Series, I-2521.

Robinson, R., and Benites, R., 1995, Synthetic seismicity models of multiple interacting faults: Journal of Geophysical Research, v. 100, p. 18,229 – 18,238.

Rousseau, C. E., and Rosakis, A. J., 2003, On the influence of fault bends on the growth of sub-Rayleigh and intersonic dynamic shear ruptures: Journal of Geophysical Research, v. 108(B9), 2411, doi:10.1029/2002JB002310.

Sharp, R. V., Lienkaemper, J. J., Bonilla, M. G., Burke, D. B., Fox, B. F., Herd, D. G., Miller, D. M., Morton, D. M., Ponti, D. J., Rymer, M. J., Tinsley, J. C., Yount, J. C., Kahle, J. E., and Hart, E. W., 1982, Surface faulting in the central Imperial valley, *in* The Imperial valley, California, earthquake of October 15, 1979: U. S. Geological Survey Professional Paper 1254, p. 119 – 144.

Sibson, R. H., 1985, A note on fault reactivation: Journal of Structural Geology, v. 7, p. 751 – 754.

Sibson, R. H., 1990, Rupture nucleation on unfavorably oriented faults, Bulletin of the Seismological Society of America, v. 80, p. 1580 – 1604.

Sibson, R. H., 1991, Loading of faults to failure: Bulletin of the Seismological Society of America, v. 81, p. 2,493 – 2,497.

Spotila, J. A., and Anderson, K. B., 2004, Fault interaction at the junction of the Transverse Ranges and Eastern California shear zone: a case study of intersecting faults: Tectonophysics, v. 379, p. 43 – 60.

Talwani, P., Amick, D. C., and Logan, R., 1979, A model to explain the intraplate seismicity in the South Carolina Coastal Plain [abs.]: Eos (Transactions, American Geophysical Union), v. 60, p. 311.

Talwani, P., 1982, Internally consistent pattern of seismicity near Charleston, South Carolina: Geology, v. 10, p. 654 – 658.

Talwani, P., 1988, The Intersection Model for Intraplate Earthquakes: Seismological Research Letters, v. 59, p. 305 - 310.

Talwani, P., and Rajendran, K., 1991, Some seismological and geometric features of intraplate earthquakes: Tectonophysics, v. 186, p. 19 – 41.

Universal Distinct Element Code, Version 3.1, 1999, ITASCA Corporation, Minneapolis, Minnesota, U.S.A.

Van Arsdale, R. B., Kelson, K. I., and Lumsden, C. H., 1995, Northern extension of the Tennessee Reelfoot scarp into Kentucky and Missouri: Seismological Research Letters, v. 66, p. 57 – 62.

Zoback, M. L., 1992, Stress Field Constraints on Intraplate Seismicity in Eastern North America: Journal of Geophysical Research, v. 97, p. 11,761 – 11,782.
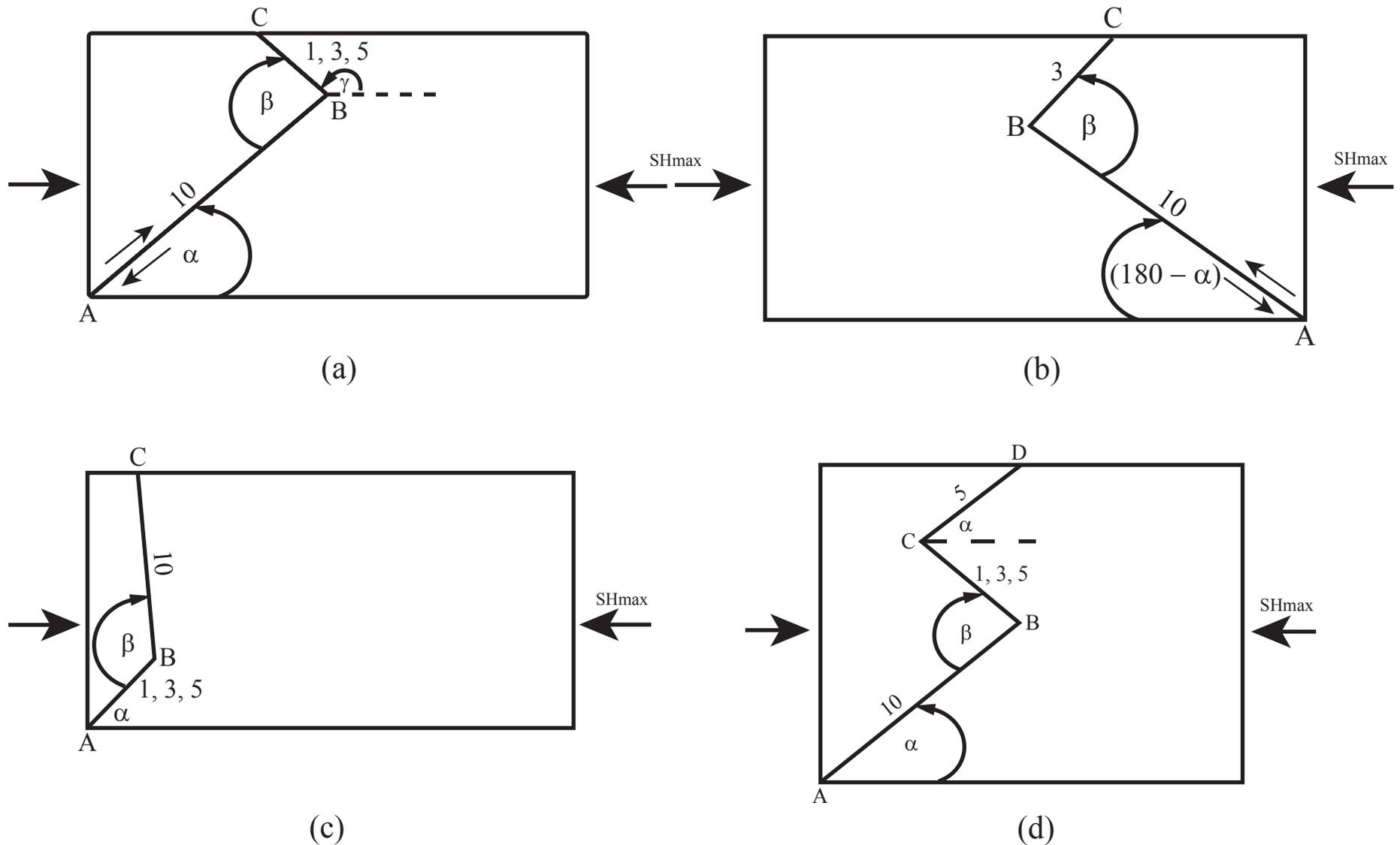
Figure 1: 2-D block geometry used to model a set of **(a)** Two intersecting faults with AB = 10 units and BC = 1, 3, 5 units **(b)** Two intersecting faults with AB = 10 units and oriented at an angle (180 - α) to S_{Hmax} and BC = 3 units **(c)** Two intersecting faults with AB = 1, 3, 5 units and BC = 10 units **(d)** a set of 3 intersecting faults with AB = 10 units, BC = 1, 3, 5 units and CD = 5 units. In all the cases, the main fault AB is oriented at an angle α to S_{Hmax} and β is the interior angle between AB and the intersecting fault BC. The angle γ is the orientation of BC with respect to S_{Hmax}. In (d) the third fault CD is oriented parallel to the main fault AB. The direction of S_{Hmax} is along the x-axis. A velocity is applied across the block, decreasing from the right to the left.
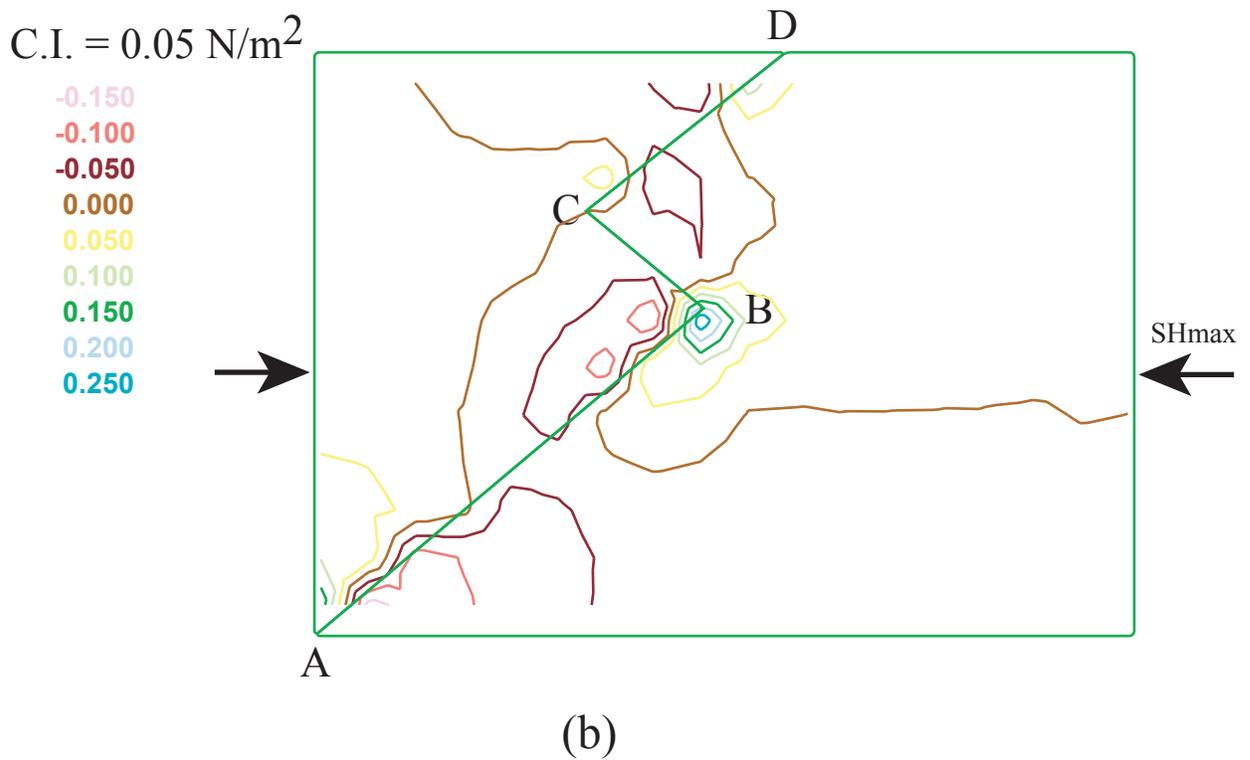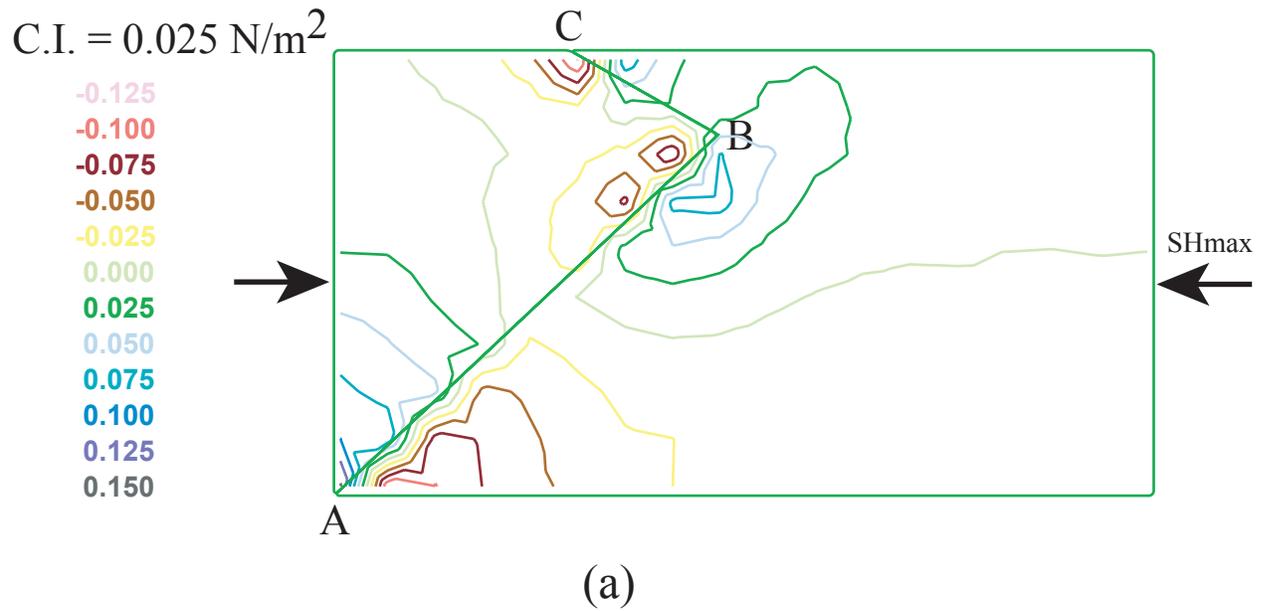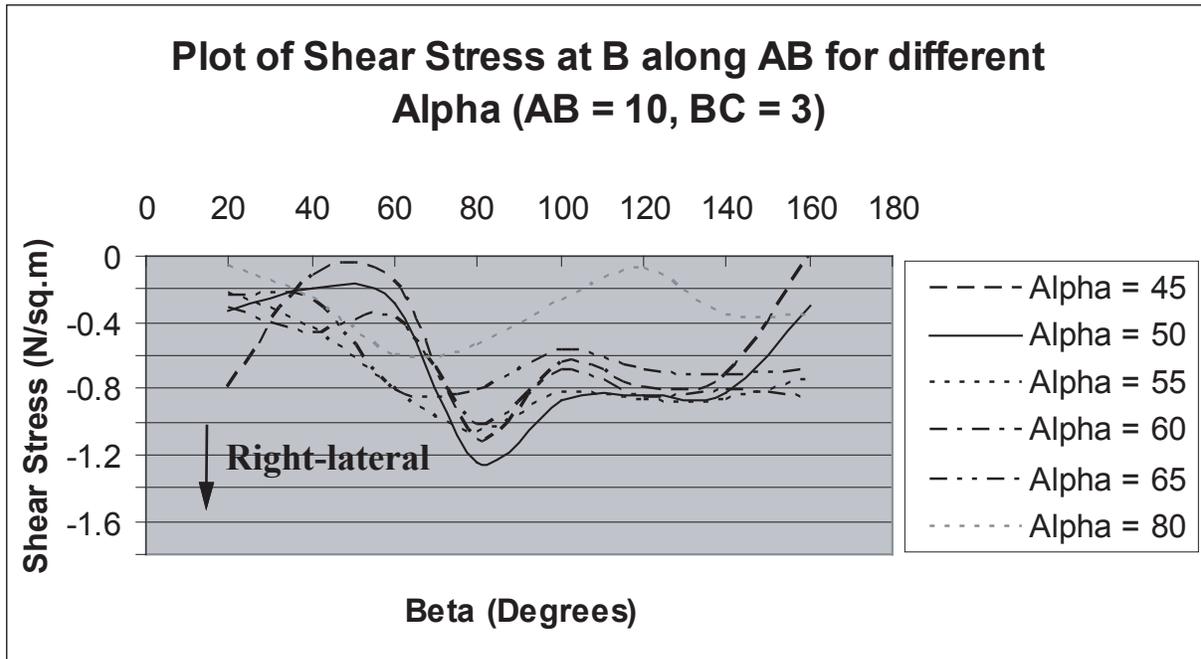
Figure 2: Contours of shear stresses are shown in plan view superimposed on the 2-D block geometry used to model a set of two intersecting faults (a) and three intersecting faults (b).
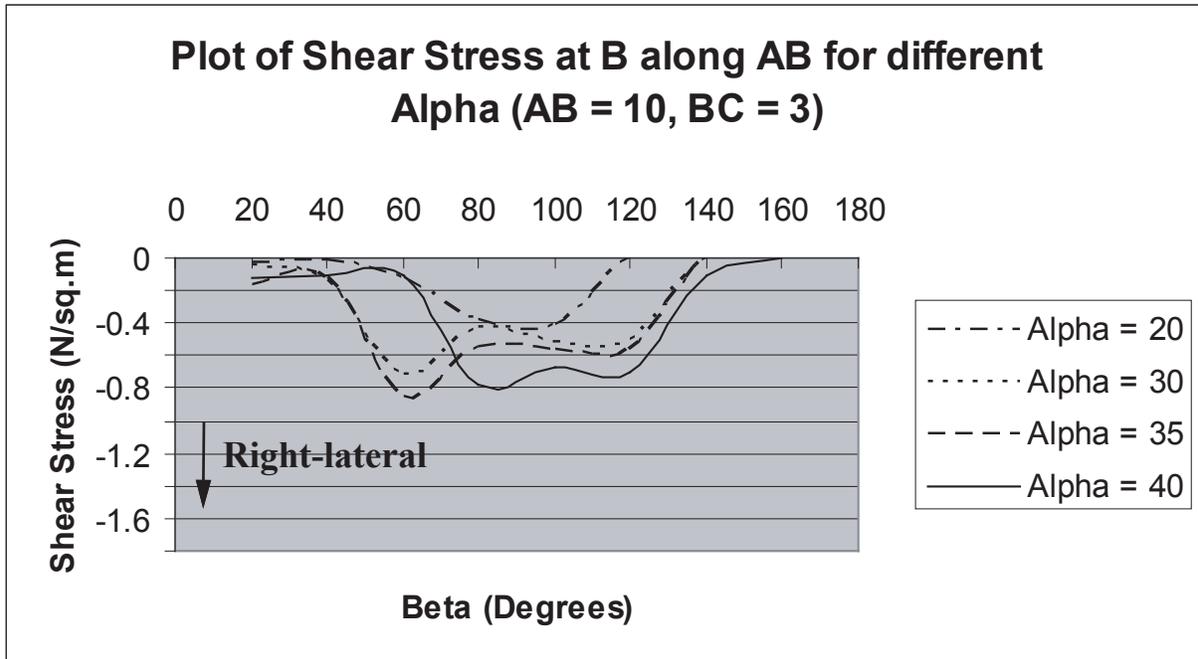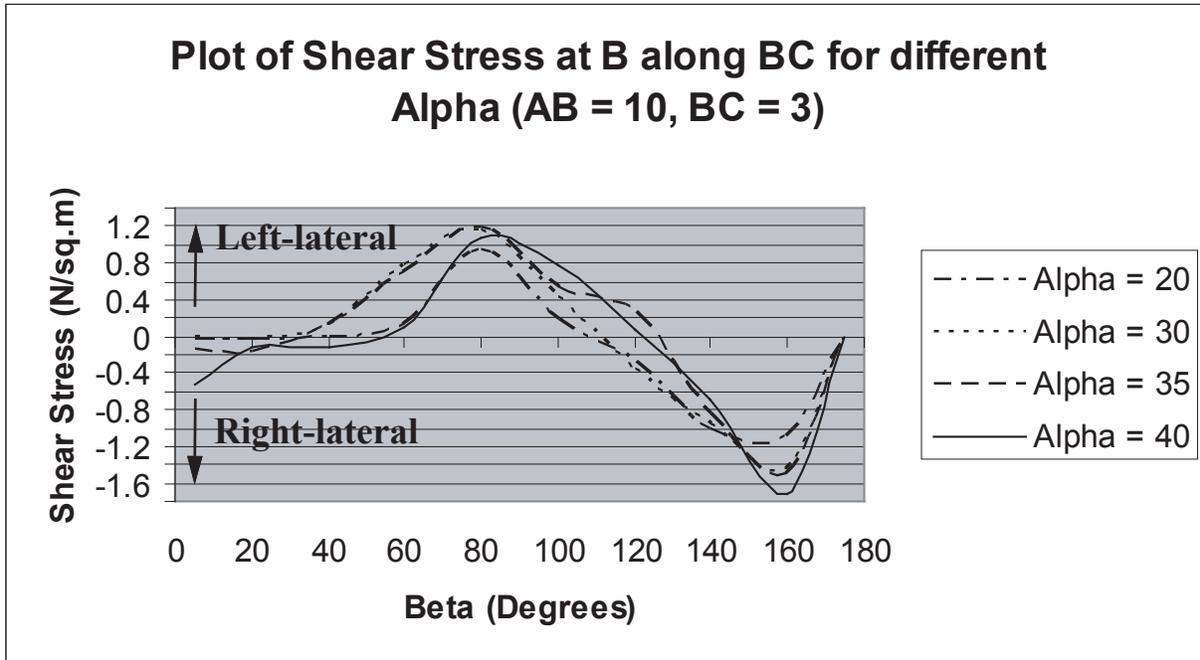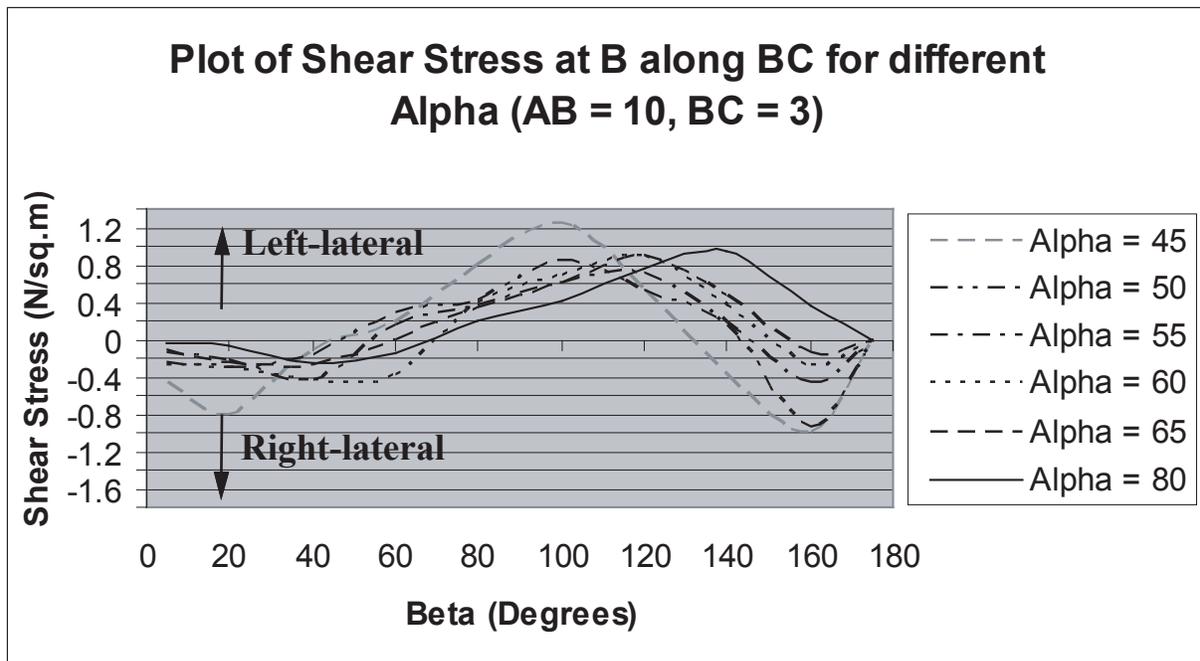
Figure 3: Plot of the magnitude of shear stress at B along fault plane AB (length = 10 units) for length of fault BC = 3 units for **(a)** α < 45 degrees and **(b)** α >= 45 degrees for a range of β = 20 to 160 degrees. The largest shear stress occurs for α = 50 degrees at β = 80 degrees.
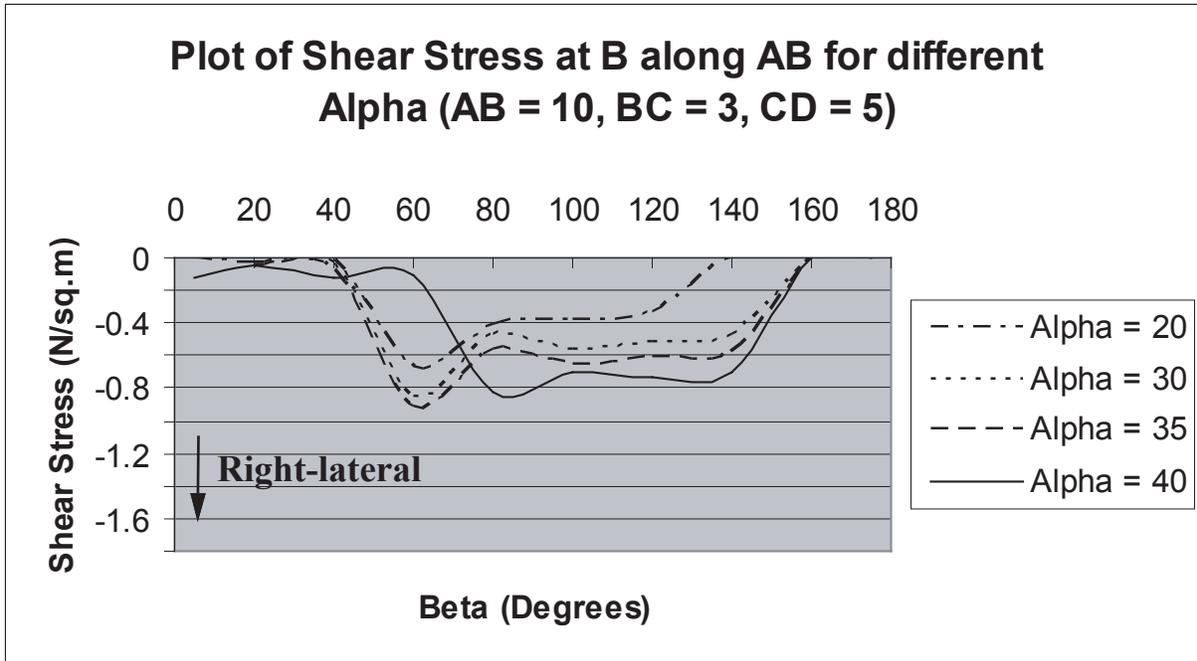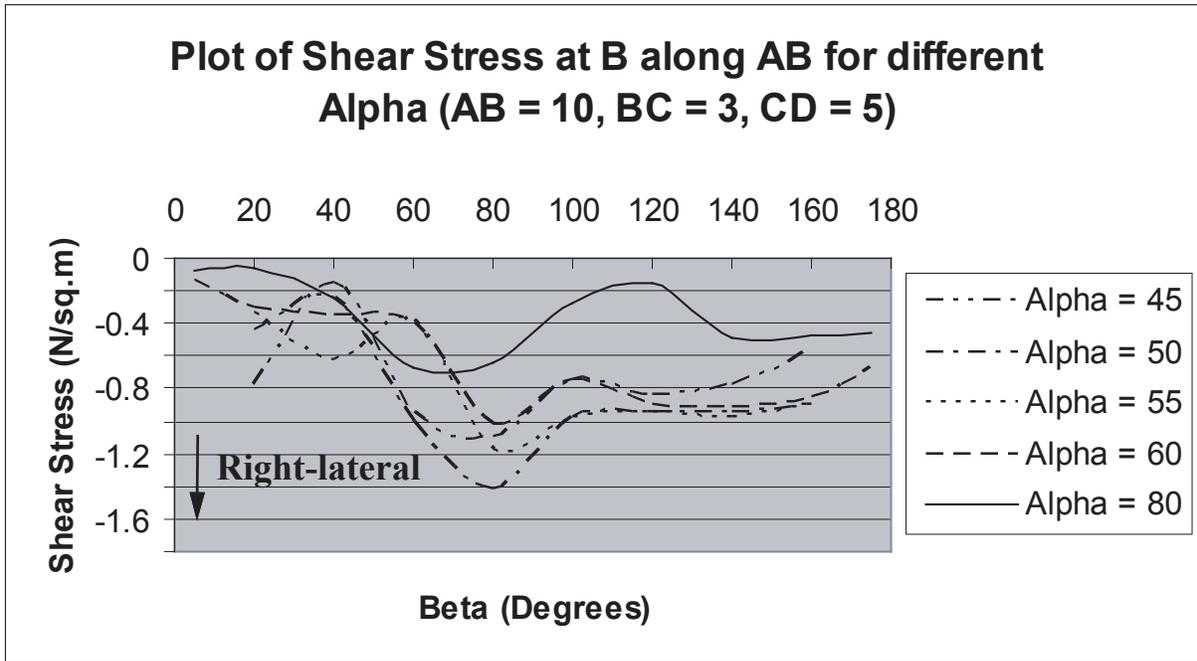
(c)

(d)

Figure 3: Plot of the magnitude of shear stress at B along fault plane BC for lengths of fault AB = 10 units and BC = 3 units for **(c)** $\alpha < 45$ degrees and **(d)** $\alpha >= 45$ degrees for a range of $\beta = 20$ to 160 degrees. The largest shear stresses in the left-lateral range occur for $\alpha = 45$ degrees at $\beta = 100$ degrees.
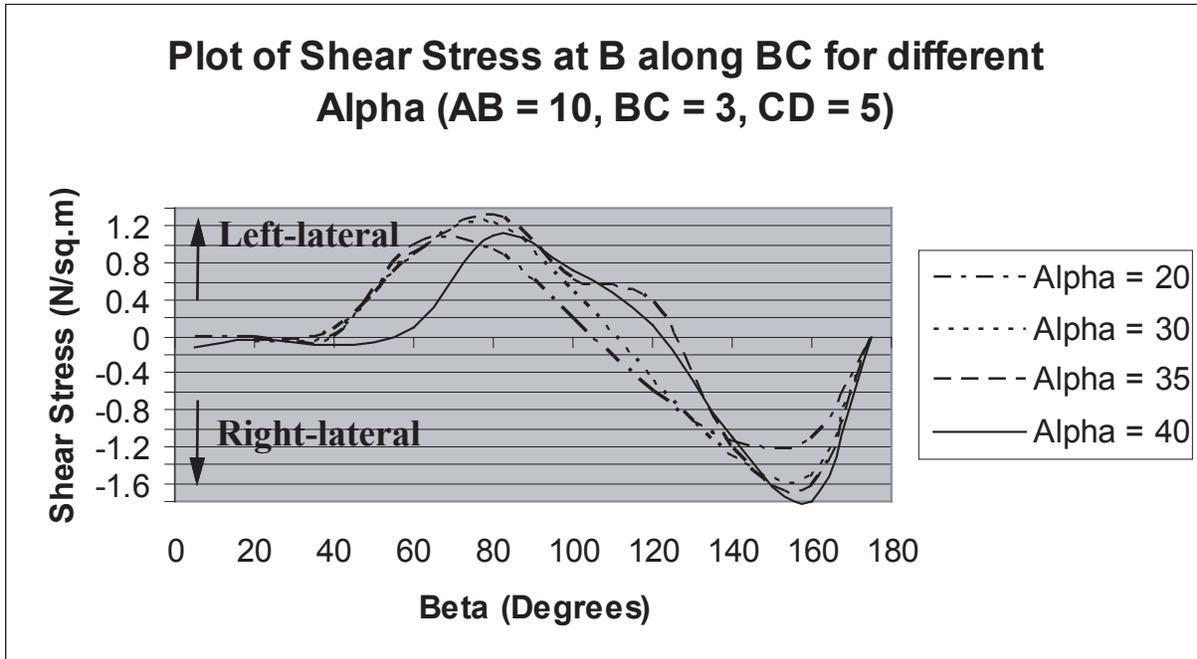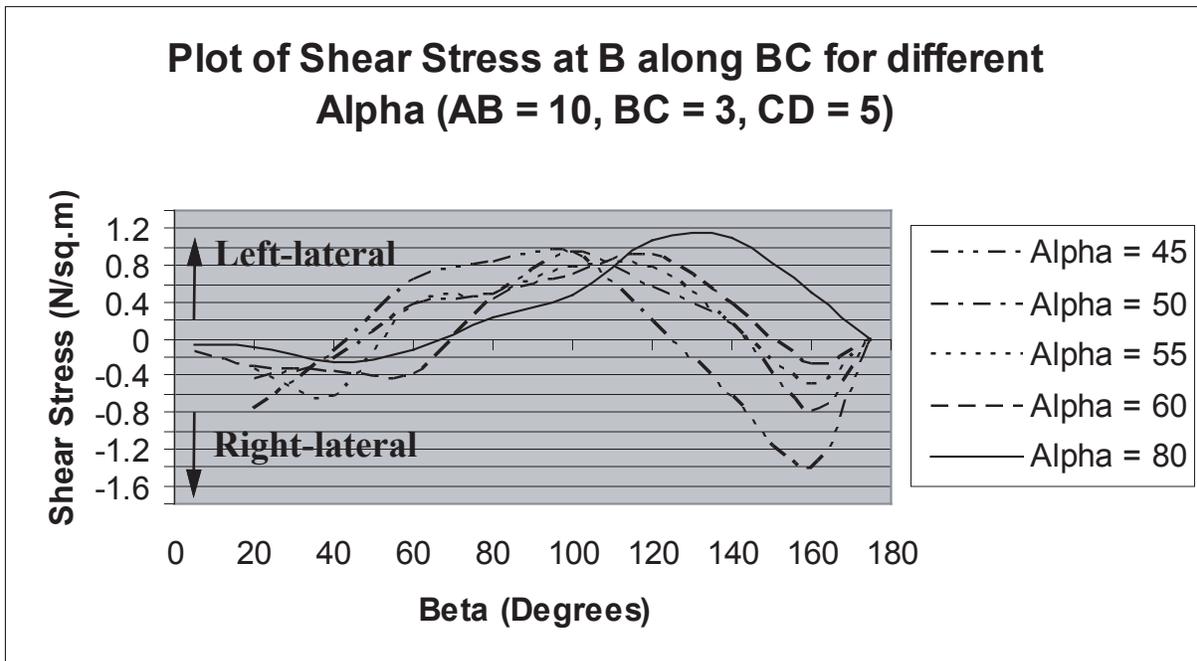
(a)

(b)

Figure 4: Plot of the magnitude of shear stress at B along fault plane AB (length = 10 units) for lengths of faults BC and CD = 3 and 5 units respectively for **(a)** α < 45 degrees and **(b)** α >= 45 degrees for a range of β = 20 to 160 degrees. The largest shear stress occurs for α = 50 degrees at β = 80 degrees.
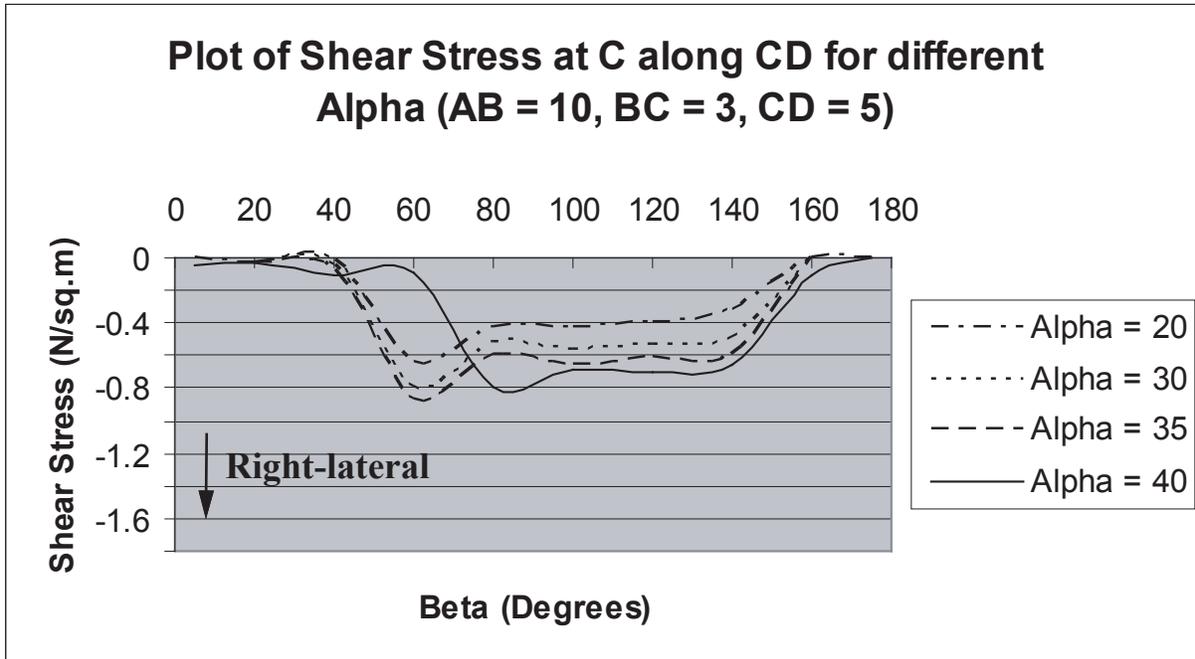
(c)

(d)

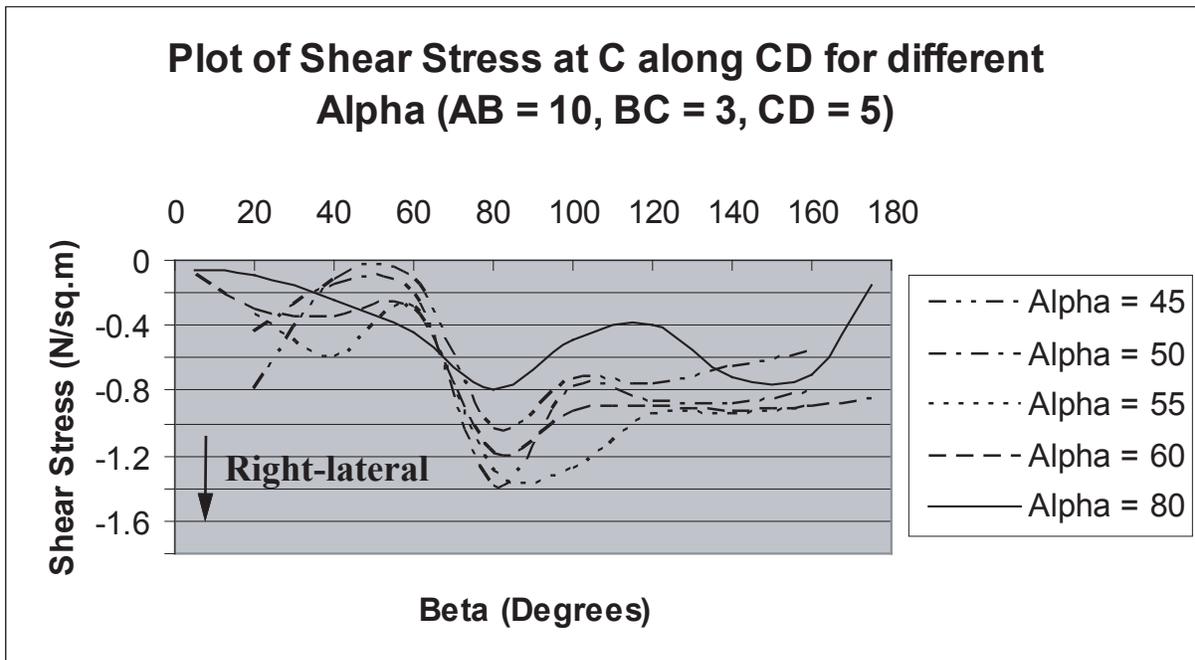**Figure 4**: Plot of the magnitude of shear stress at B along fault plane BC for lengths of faults AB, BC, and CD = 10, 3, and 5 units respectively for **(c)** $\alpha < 45$ degrees and **(d)** $\alpha >= 45$ degrees for a range of $\beta = 20$ to 160 degrees. The largest shear stress in the left-lateral range occurs for $\alpha = 35$ degrees at $\beta = 80$ degrees.
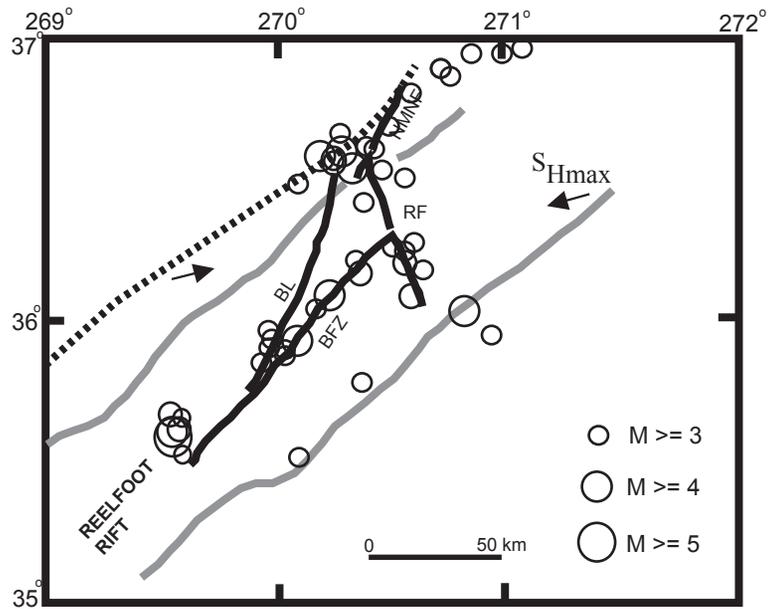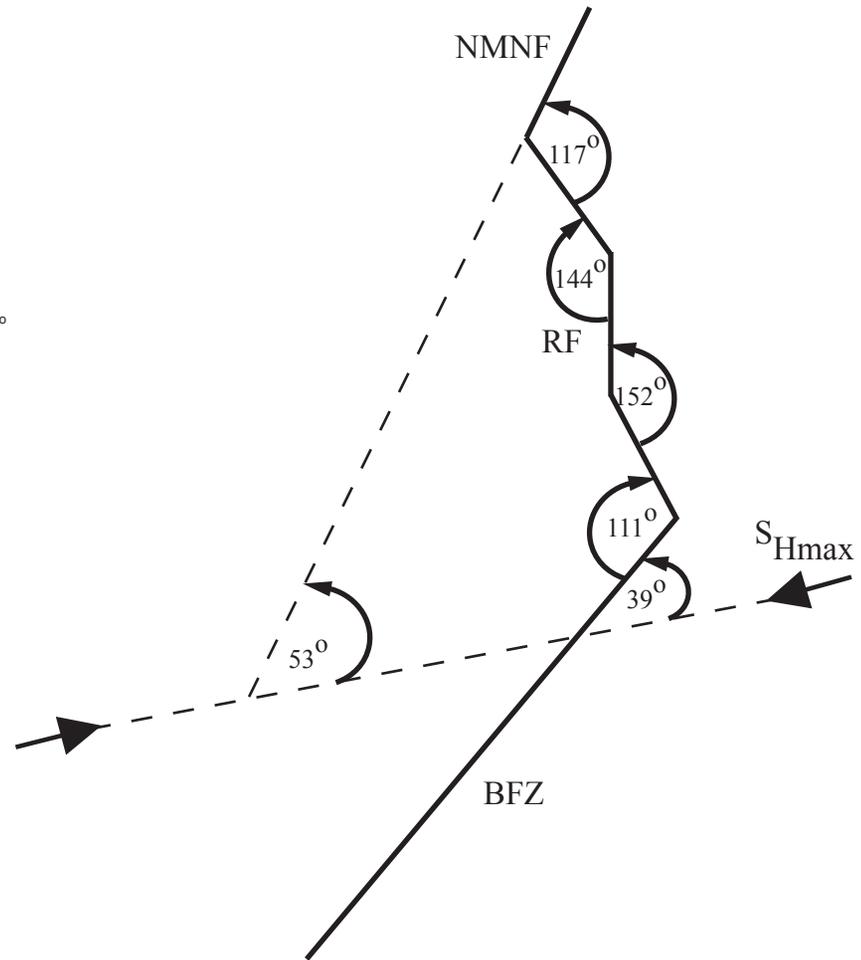
(e)

(f)

Figure 4: Plot of the magnitude of shear stress at B along fault plane AB (length = 10 units) for lengths of faults BC and CD = 3 and 5 units respectively for **(e)** α < 45 degrees and **(f)** α >= 45 degrees for a range of β = 20 to 160 degrees. The largest shear stress occur for α = 50 degrees at β = 80 degrees.

Figure 5: (a) Map showing New Madrid Seismic Zone. The margins of the Reelfoot rift floor (solid grey lines), and faults (solid black lines) have been taken from Hildenbrand et al. (2001). The edge of the western margin of the Reelfoot rift (dotted line) has been adopted from Rhea and Wheeler (1995). BFZ - Blytheville Fault Zone, RF - Reelfoot fault, NMNF - New Madrid North fault, BL - Bootheel Lineament. Open circles represent instrumentally located seismicity of M >= 3.0 from 1974 - 2002 from CERI, Memphis catalog. (b) Schematic representation of the seismogenic faults in NMSZ (not to scale). BFZ and NMNF are oriented at angles α_1 and α_2 counterclockwise with respect to S_{Hmax} (bold arrows). Based on the analyses of seismicity by Pujol et al. (1997), the Reelfoot fault has been divided into three segments that make angles β_1, β_2, and β_3 with BFZ.
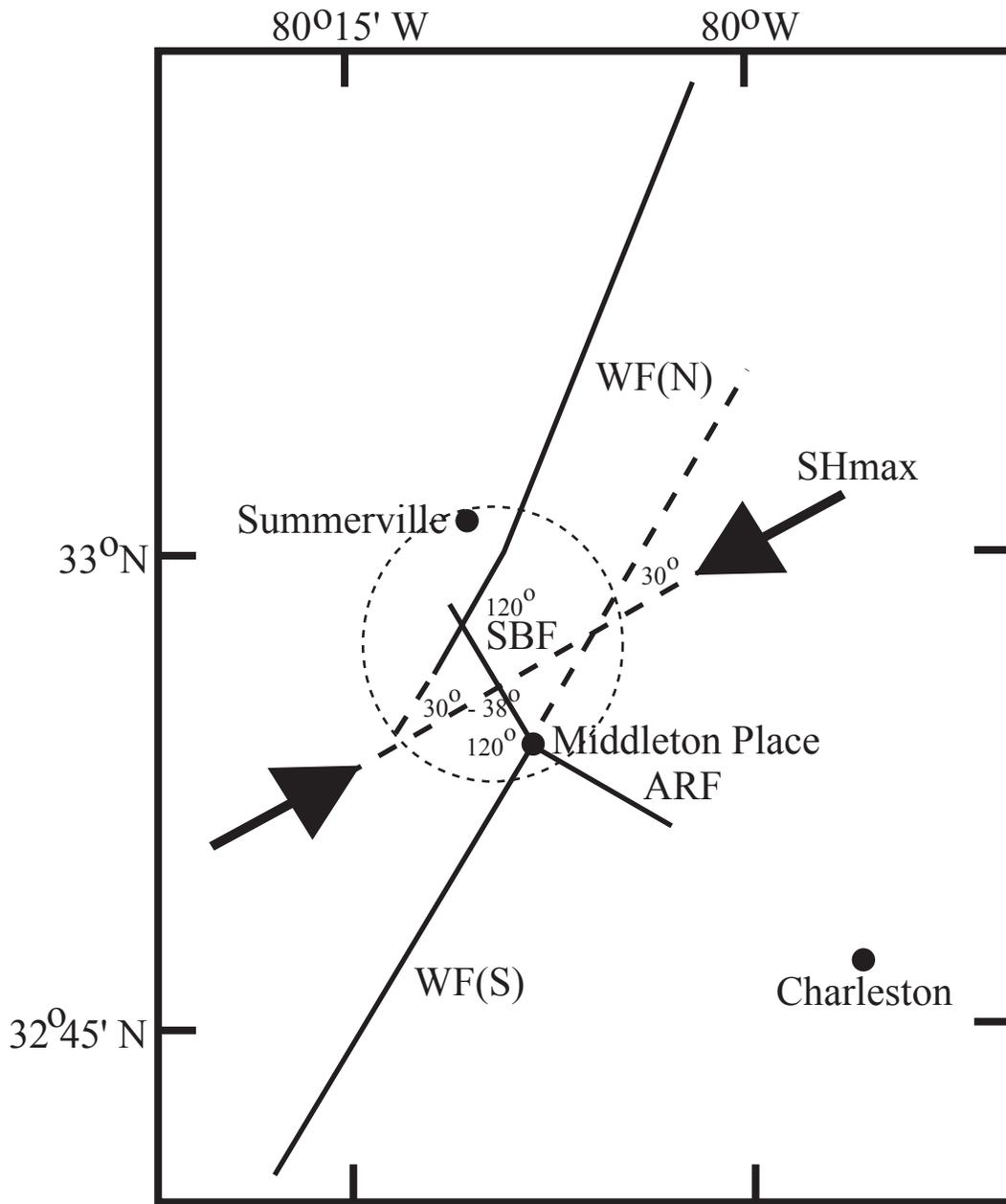
Figure 6: Map showing Middleton Place Summerville Seismic Zone (MPSSZ). The seismogenic faults (solid black lines) have been taken from Dura-Gomez (2004). WF(N) - Woodstock fault North, SBF - Sawmill Branch Fault, ARF - Ashley River Fault, WF(S) - Woodstock fault South. The dashed circle outlines the area of instrumentally located seismicity. The orientations of WF(N) and WF(S) (α_1 and α_2) with respect to S_{Hmax} (bold arrows) are shown together with the interior angles subtended by SBF (β_1), and ARF (β_2).
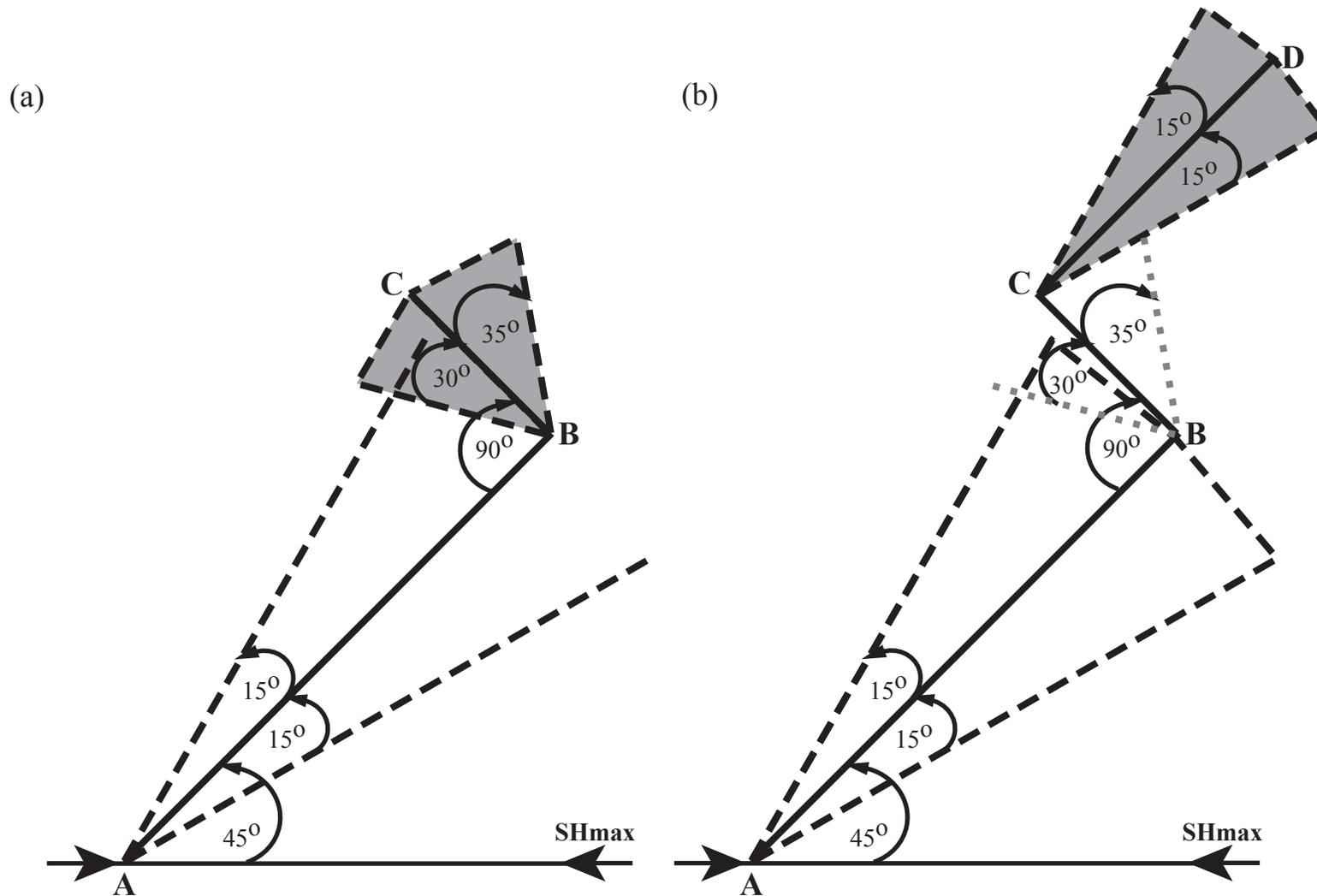
Figure 7: Cartoon showing summary of the modeling results with (a) two and (b) three intersecting faults. The favorable range for orientation of the main fault AB with respect to S_{Hmax} was found to be ~45° +/- 15° in (a) and (b)]. A similar range for orientation of fault CD with respect to S_{Hmax} was also obtained [light gray shaded area in (b)]. The range of β that yielded maximum shear stresses at the intersection was ~90° +/- 35°, light gray shaded area in (a) and area bounded by light gray small-dotted line in (b)] when the motion along the intersecting fault BC was opposite that along the main fault AB.

Table 1: Summary of Preferred Angles of Orientation (α and β) from Model Results													
GEOMETRY	**Figure**	**AB**	**BC**	**OBSERVATIONS AT B ALONG AB**					**OBSERVATIONS AT B ALONG BC(*)**				
		(Length Units)	(Length Units)	Maximum			Favorable Range (90% Max. Value)		Maximum			Favorable Range (90% Max. Value)	
				Shear Stress (N/sq.m)	α (Deg)	β (Deg)	α (Deg)	β (Deg)	Shear Stress (N/sq.m)	α (Deg)	β (Deg)	α (Deg)	β (Deg)
2 Intersecting Faults	1a	10	1	-1.03	60	80	45 - 60	75 - 100	1.1	45	120	35 - 45	65 - 125
									-1.55	40	160	35 - 40	152 - 164
			3	-1.25	50	80	46 - 53	76 - 91	1.25	45	100	30 - 45	75 - 105
									-1.72	40	160	37 - 41	153 - 170
			5	-1.58	50	80	48 - 52	75 - 89	1.45	30	80	30 - 37	68 - 85
									-1.87	40	160	36 - 42	149 - 162
2 Intersecting Faults	1b	10	3	1.32	130	80	127 - 134	75 - 90	-1.18	145	80	140 - 150	70 - 85
									1.64	140	160	137 - 143	152 - 170
2 Intersecting Faults	1c	1	10	-1.19	45	80	45 - 60	70 - 95	1.05	30	80	30 - 37	70 - 85
									-1.48	30	160	35 - 40	150 - 164
			3	-1.32	45	80	45 - 50	70 - 84	1.24	30	80	30 - 35	72 - 84
									-1.8	40	160	33 - 42	151 - 162
			5	-1.52	45	80	47 - 52	75 - 87	1.4	30	80	30 - 34	67 - 85
									-1.87	40	160	35 - 42	150 - 164

*Positive values for left-lateral region and negative values for right-lateral region

Table 2: Summary of Preferred Angles of Orientation (α and β) from Model Results																		
GEOMETRY	**AB**	**BC**	**CD**	**OBSERVATIONS AT B ALONG AB**					**OBSERVATIONS AT B ALONG BC(*)**					**OBSERVATIONS AT C ALONG CD**				
	(Length Units)	(Length Units)	(Length Units)	**Maximum**			**Favorable Range**		**Maximum**			**Favorable Range**		**Maximum**			**Favorable Range**	
							(90% Max. Value)					**(90% Max. Value)**					**(90% Max. Value)**	
				Shear Stress	**α**	**β**	**α**	**β**	**Shear Stress**	**α**	**β**	**α**	**β**	**Shear Stress**	**α**	**β**	**α**	**β**
				(N/sq.m)	**(Deg)**	**(Deg)**	**(Deg)**	**(Deg)**	**(N/sq.m)**	**(Deg)**	**(Deg)**	**(Deg)**	**(Deg)**	**(N/sq.m)**	**(Deg)**	**(Deg)**	**(Deg)**	**(Deg)**
3 Intersecting Faults	10	1	5	-1.19	50	80	45 - 60	65 - 95	1.25	35	80	30 - 40	65 - 90	-0.15	50	80	45 - 60	70 - 105
(Figure 1d)									-1.595	40	160	35 - 40	145 - 166					
		3	5	-1.42	50	80	48 - 53	69 - 89	1.32	35	80	30 - 38	68 - 85	-1.39	50	80	48 - 56	76 - 103
									-1.8	40	160	34 - 42	150 - 163					
		5	5	-1.65	50	80	48 - 53	74 - 87	1.41	35	80	32 - 38	70 - 85	-1.48	50	80	48 - 52	70 - 100
									-2.1	40	160	36 - 42	150 - 164					
*Positive values for left-lateral region and negative values for right-lateral region																		